ACS OMEGA

http://pubs.acs.org/journal/acsodf

Article

Carbon Nanotubes Decorated with Coordination Polymers for Fluorescence Detection of Heavy-Metal Ions and Nitroaromatic Chemicals

Mansour A.S. Salem, Amjad Mumtaz Khan,* Yahiya Kadaf Manea, Hatem A.M. Saleh, and Musheer Ahmad

Cite This: *ACS Omega* 2023, 8, 1220−1231

Read Online

ACCESS | Metrics & More | Article Recommendations | Supporting Information

ABSTRACT: Herein, $[Nd(NO_3)_3(H_2pzdca)]_n$ (MA-1) was synthesized from a reaction of 2,3-pyrazinedicarboxylic acid [H_2Pzdca] as an organic linker with salt of Nd(III) under solvothermal conditions. The detailed structural analysis for crystals was performed utilizing single-crystal X-ray diffraction (SCXRD). After that, the neodymium-based coordination polymer (MA-1) crystal was directly generated upon the surface of functionalized carbon nanotubes (F-CNTs) through bonds or affinity between F-CNTs and MA-1 via the solvothermal approach. Meanwhile, the existence of F-CNTs does not affect the production of MA-1 crystals. FT-IR, PXRD, SEM, TEM, and SCXRD studies were used to characterize the crystalline material, MA-1 and MA-1@CNT. To investigate the MA-1@CNT sensing properties, Pb(II), As(III), Cr(VI), and nitrobenzene (NB) were utilized as analytes. It is worth mentioning that MA-1@CNT developed as a susceptible sensor exhibits a fluorescence "turn-on" response for Pb(II) and As(III) ions, while a fluorescence "turn-off" response in the case of Cr(VI) and NB with significantly low limit of detection (LOD) values of 15.9 for Pb(II), 16.0 for As(III), 76.9 for Cr(VI), and 21.1 nM for NB, which are comparable with the lowest LOD available in the literature. Furthermore, MA-1@CNT could be conveniently regenerated and reused for at least three cycles by simply filtering and washing with water several times. The sensing mechanism is ascribed to the inner filter effect owing to the overlap between the emission and/or excitation bands of MA-1@CNT with the absorption bands of Cr(VI) and NB. In contrast, the fluorescence enhancement in the case of Pb(II) and As(III) could be correlated to the chelation-enhanced fluorescence phenomenon. These results indicate that MA-1@CNT is an ideal sensor for Pb(II), As(III), Cr(VI), and NB recognition.

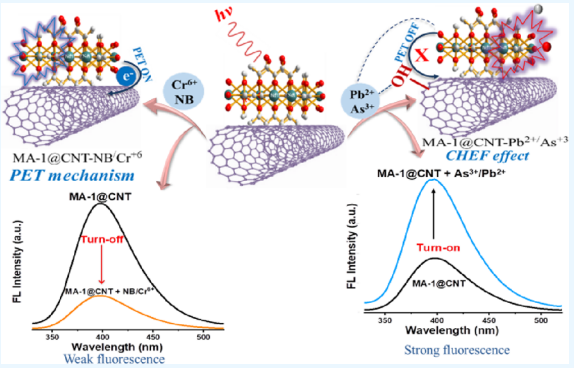

1. INTRODUCTION

Environmental contaminants have increased dramatically throughout the past few decades owing to industrial expansion and significant population growth.[1,2]

In our everyday lives, chromium is extensively employed as an industrial material, particularly in the tanning industries, plastics, production of pigment dyes, metallurgy, ceramics, protective coating, and electroplating. Fundamentally, there are two stable oxidation states of chromium, Cr(III) and Cr(VI). Humans require Cr(III), which is essential for insulin action as well as protein, glucose, and lipid metabolism. Additionally, chromium-(VI) can impair the human immune system (hematological, respiratory, and gastrointestinal), and it is highly carcinogenic. Due to its very soluble nature, Cr(VI) is mobile and bioavailable in aqueous systems.[3−6]

Like other heavy metals, arsenic is very toxic even in trace amounts because biological ligands that include oxygen, nitrogen, and sulfur have a high proclivity to bind with this deadly metal ion, resulting in enzyme inhibition and changes in the molecular structure of proteins or breakdown of hydrogen bonds. Arsenic is present in two forms in natural water: arsenite As(III) and arsenate As(V). Both inorganic species of arsenic are harmful to human health, producing skin sores on the chest, hands, and feet and eventually leading to cancer if left untreated. As(III) is the more hazardous of the two forms for biological systems.[7,8]

Meanwhile, due to their high demand worldwide, nitro-aromatic compounds (NACs) are widely employed in various industries and are synthesized in huge quantities. The widespread use of NACs creates a severe pollution risk. In the same context, lead Pb(II) is highly harmful to humans when available in high concentrations in water. As heavy metals,

Received: October 15, 2022
Accepted: December 8, 2022
Published: December 21, 2022

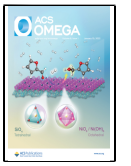

Pb(II) ions are gaining wide interest among researchers since all forms of Pb(II) are hazardous and harmful to the development process in children's nervous, reproductive, immune, and cardiovascular systems.[9] Nitrobenzene (NB) is a deadly contaminant commonly emitted by chemical industries, polluting soil and water sources. A minimal dose of NB is exceedingly hazardous to human health and is carcinogenic, causing vomiting, shortness of breath, and nausea. Hence, the United States Environmental Protection Agency (USEPA) has listed NB as a severe water pollutant and classified it as a B2 carcinogen.[10] NB has been used in the industrial production of plastics, pesticides, and explosives, but its detection is essential for being toxic.[11,12]

For these reasons, various modern conventional methods have been used to detect NB and Cr(VI) from polluted aquatic environments, notably UV−vis spectrometry, electrochemical technique, chromatography, and luminescence. Among these methods, fluorescence detection is thought to be the most effective due to its remarkable sensitivity and affordable cost.[13−15] In this context, there was a pressing need to create novel nanomaterials that could detect Pb(II), As(III), Cr(VI), and NB in aqueous mediums. Presently, a number of recent studies have been conducted by fluorescence detection on the basis of mixed-ligand-based robust cadmium(II)-frameworks,[16] amine-decorated multifunctional luminescent metal−organic frameworks,[17] transition metal coordination polymers based on bent carboxylate and flexible spacer ligands,[18] pillar-bilayer cadmium(II) frameworks,[19] etc. In order to meet these challenges, new nanocomposites have been used to detect contaminants in water.

In this respect, coordination polymers (CPs) first appeared in the mid-1990s as a nanostructured porous material when Yaghi et al. started developing molecules that could be created using a wide assortment of organic substances and metal ions. The innovation for synthesizing CPs by self-assembling the organic ligands with inorganic metal cations produces a framework in a suitable topology. Afterward, CPs attracted interest of many researchers due to their distinct features, which include a large surface area, crystalline structure, chemical tenability, open metal sites, and extra high porosity.[20,21]

Correspondingly, carbon nanotubes (CNTs) are regarded as promising precursors for the synthesis of composites, and they possess outstanding flexibility, high mechanical strength, chemical stability, high mechanical strength, and excellent electrical conductivity.[22,23] However, CNTs are hydrophobic, entangle with one another, and preferentially aggregate, just like many other nanomaterials. Several surface modification procedures have been explored to eliminate interfacial imperfections and enhance the quality of CNT dispersion in the polymer matrix. Grafting functional groups onto the external surface of CNTs is one viable option, which is commonly accomplished by strong acid treatment. Aside from metal doping or grafting organic functional groups, another option is to decorate CPs onto CNTs.[24,25]

While CPs have interesting physical and chemical features for a wide variety of applications, their characteristics can be easily improved by changing their structure as well as physicochemical nature using grafting with active functional groups,[26] substituting organic linkers,[27] attempting to make composites with various materials,[28,29] and impregnating them with suitable materials.[30] This field is still in its early stages, and various publications on the synthesis and future uses of CPs composites have lately been published.[31,32] However, finding synthetic pathways and appropriate complementary materials are essential for producing CP-based composites.

CNTs are one of the ideal materials for producing CP composites, which enhance CP formation by suppressing their aggregation, raising scattering forces within the CPs, and controlling CP features, including structure, morphology, and size.[33]

Based on these features, CPs can potentially be applied in various industrial and research fields, including catalysis, sensing, drug delivery, gas separation/storage, energy storage/conversion, etc.[1,33,34] Therefore, CP@CNT composites were expected to be smart materials for the detection of hazardous compounds, viz. Pb(II), As(III), NB, and Cr(VI).

We have successfully synthesized the Nd-CP@CNT (MA-1@CNT) composite by employing the F-CNT as a base for the in situ Nd-CP growth using a simple hydrothermal approach. Therein, H_2pzdca is used as a linker for Nd-CP. The CH_2O and OH^- groups on the F-CNT surface function as binding sites for Nd(III) at the start of the reaction, resulting in nucleation and probable priority for Nd-CP crystal formation on the F-CNT surface. The physicochemical parameters of the resultant MA-1@CNTcomposite were determined by several approaches, such as FT-IR, XRD, TEM, SEM, and SCXRD. As expected, three-dimensional (3D) Nd-CP nanorods grow on the F-CNT surface to make a flower-like MA-1@CNT nanocomposite. Additionally, it is concluded that incorporating such CPs with CNTs provides a vast surface area, allowing more analyte moieties to be touched and thereby facilitating excellent sensitivity, which is applied as a sensor against various hazardous compounds. The luminescent features of MA-1@CNT disseminated in different solvents have been studied systematically, showing extremely selective aqueous phase sensing of Pb(II), As(III), Cr(VI), and NB with a higher limit of detection limit (LOD).

2. EXPERIMENTAL SECTION

2.1. Chemicals and Reagents. Sigma-Aldrich Chemical Co. India supplied carbon nanotubes, neodymium(III) nitrate [$Nd(NO_3)_3{\cdot}6H_2O$], 2,3-pyrazinedicarboxylic acid [H_2pzdca], *N*,*N*-dimethyl formamide [DMF], nitrobenzene [$C_6H_5NO_2$], potassium dichromate [$K_2Cr_2O_7$], dimethyl sulfoxide [DMSO], methanol, ethanol, and sodium chloride [NaCl], which were used without further purification.

2.2. Oxidization of MWCNTs. The acid treatment of pristine CNTs yielded F-CNTs, where MWCNTs were ultrasonically dispersed for 30 min in 6 M HNO_3 and further shaken by a magnetic stirrer at 60 ± 2 °C till dry. Subsequently, the black solid was filtered, thoroughly rinsed with deionized water (DW), and dried for 12 h at 60 ± 2 °C.[35]

2.3. Synthesis of $[Nd(NO_3)_3(H_2pzdca)]_n$ or MA-1. DMF (2 mL) was used to dissolve H_2pzdca (0.0338 g, 0.2 mmol) and mixed with $Nd(NO_3)_3{\cdot}6H_2O$ (0.0438 g, 0.1 mmol) with further addition of H_2O (2 mL). The mixture was placed in a Teflon-lined autoclave, and the reaction was maintained for 48 h at 130 ± 2 °C. White crystals were obtained with 58% yields. Elemental analysis (%) for MA-1: calc., C = 27.24, H = 0, N = 0; found for C_7NdO_5 (MA-1): C = 27.17, H = 0, N = 0.

2.4. Synthesis of MA-1@CNT Nanocomposites. In a typical assay, 0.5 mg of F-CNTs was first dissolved in 4 mL of DMF-H_2O (1:1) solution at ambient temperature and under ultrasonication to form a homogeneous black suspension. Then, $Nd(NO_3)_3{\cdot}6H_2O$ (0.0438 g,0.1 mmol) and H_2pzdca (0.0338 g, 0.2 mmol) were added to F-CNT suspensions described above

https://doi.org/10.1021/acsomega.2c06209
ACS Omega 2023, 8, 1220−1231

Scheme 1. Synthesis of MA-1 and MA-1@CNTs

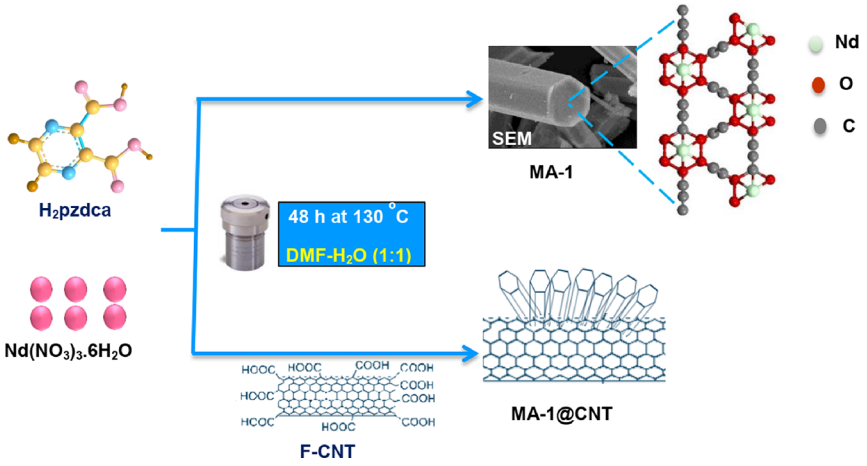

followed by 1 h of stirring to form a new suspension. The resulting mixture was put in a 5 mL Teflon-lined autoclave in an oven for 48 h at 130 ± 2 °C. After cooling at RT, the product was washed after being collected with excess ethanol and deionized water until neutral. Lastly, the precipitates were dried at 60 ± 2 °C for 12 h to form MA-1@CNT. The synthesis procedure is depicted schematically in (Scheme 1).

2.5. Methods and Instruments. FT-IR employing the KBr disk method was utilized to determine the functional groups in the samples in the range 400−4000 cm^{-1}. The (XRD, Shimadzu 6100) instrument diffractometer was used to perform XRD using Cu Kα radiation (1.54 nm). The materials' morphologies were investigated using SEM (JSM-6510LV, JOEL Japan). TEM examination was performed on a JEOL-JEM2100. The FL spectra were obtained using a Hitachi spectrofluorimeter (F-2500). At ambient temperature, absorption spectroscopic measurements were taken with a Perkin Elmer Lambda-45 UV−vis spectrophotometer.

2.6. X-ray Crystal Structure Determination. MA-1 SCXRD data were collected at 293 (2) K using Mo Kα radiation (λ = 0.71073 Å) on a Rigaku XtaLAB Synergy-i diffractometer. Using Olex2,[36] the structure was solved with the Olex2.solve[37] structure solution program using Charge Flipping and refined with the Olex2.refine[37] refinement package using Gauss−Newton minimization.

3. RESULTS AND DISCUSSION

3.1. Structural Descriptions of MA-1. Refinement parameters and crystal data for MA-1 are provided in Table 1, while bond lengths and angles are reported in Tables S1 and S2. The SCXRD data show that MA-1 crystallizes in a monoclinic space group with a $C2/c$ space group. The ball-and-stick model of MA-1 is depicted in Figure 1a. The crystal structure of synthesized MA-1 reveals a 3D network, where the asymmetric unit of MA-1 (C_7NdO_5) has a single neodymium ion and a moiety of the linker H_2pzdca due to the cracking process of the linker as shown in Figure 1b. Four oxygen atoms come from three completely deprotonated (H_2pzdca) ligands, one oxygen atom from one coordinated water, and one carbon from the ligand, which is brokenly coordinated to Nd1 (Figure 1c). The coordination polyhedron is depicted in Figure 1d. The 3D interpenetrated layer of MA-1 is shown in Figure 2. The bond lengths of Nd1-O1 and Nd1-O2 are 1.577 and 2.586 Å, respectively.

Table 1. Summary of Crystallographic Data for MA-1

	MA-1
empirical formula	C_7NdO_5
formula weight	308.31
crystal system	monoclinic
space group	$C2/c$
color	white
a, Å	6.2712(4)
b, Å	10.6104(5)
c, Å	8.1233(5)
A	90
B	102.451(6)
Γ	90
V/Å^3	527.81(5)
$P_{(calc)}$ g·cm^{-3}	7.7593
Z	8
$F(000)$	1136.4
μ/mm^{-1}	19.616
index ranges	$-7 \le h \le 7 - 13 \le k \le 13 - 10 \le l \le 10$
reflections collected	4015
independent reflections	568 [R_{int} = 0.0628, R_{sigma} = 0.0329]
R indexes [$I \ge 2\sigma(I)$]	R_1 = 0.0483, wR_2 = 0.1171
R indexes [all data]	R_1 = 0.0772, wR_2 = 0.2853
goodness-of-fit on F^2	1.432

3.2. Material Characterizations. XRD, FT-IR, SEM, and TEM methods were used to evaluate MA-1 and MA-1@CNT thoroughly.

3.2.1. XRD Analysis. The crystal structure of simulated MA-1, F-CNT, MA-1, and MA-1@CNT was analyzed by powder XRD (Figure 3a). The characteristic diffraction peaks of MA-1@CNT appear at 2θ = 17.1°, 23.6°, 26.1°, 28.9°, 33.7°, 41.8°, 45.5°, and 48.6°, which are well consistent with the XRD pattern of the MA-1 crystal. In contrast, the peak at 26.1° is the characteristic of the F-CNT; it demonstrates that the functional groups are stabilized on the tube wall and that the overall structure of the carbon tube was not destroyed. The high intensity of the significant peaks suggests highly crystallized materials. In the MA-1@CNT composite, the peak of F-CNT and most diffraction peaks for MA-1 can be seen, and this indicates that the F-CNT does not destroy the MA-1 skeleton. As it is evident, all peaks of the composite were decreased compared to MA-1, and the crystalline sizes of MA-1 and MA-1@CNT calculated by the Debye−Scherrer equation were 94.9 and 59.5 nm,

https://doi.org/10.1021/acsomega.2c06209
ACS Omega 2023, 8, 1220−1231

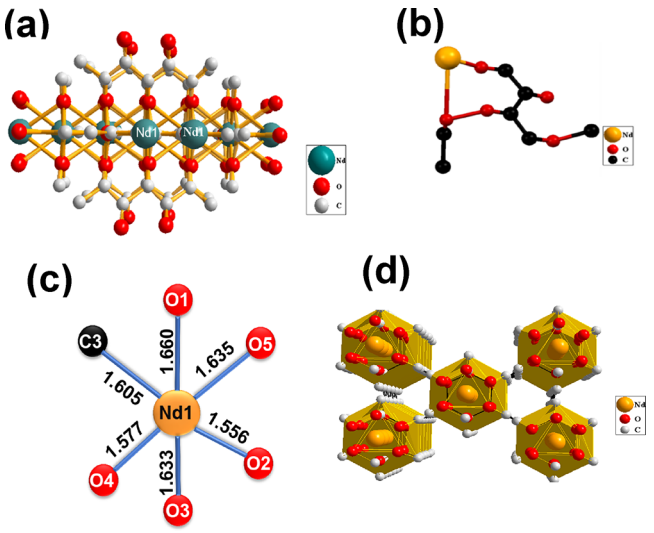

Figure 1. (a) Ball-and-stick model of MA-1, (b) asymmetric unit of MA-1, (c) coordination environment of Nd1 in MA-1, and (d) coordination polyhedron of MA-1.

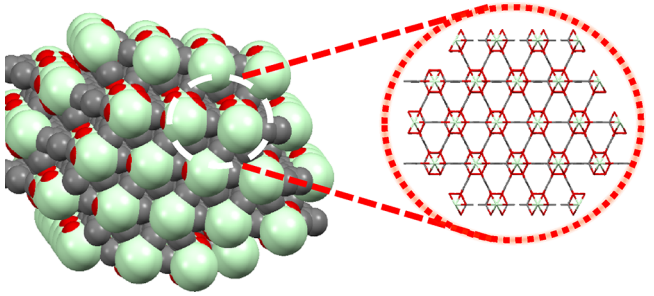

Figure 2. 3D interpenetrated layer of the MA-1 and its simplified layer (inset).

respectively. All these indications confirm the existence of the CNT in the composite.

3.2.2. FT-IR Spectral Analysis. The chemical structures of MA-1 were described using the FT-IR spectrum and its composite with F-CNT. As depicted in Figure 3b, all the peaks of MA-1 were existent in the composite, indicating that the F-CNT incorporation did not affect the chemical structure of MA-1.[38] The peak positions at 3486 and 2923 cm^{-1} demonstrate the presence of an O−H stretching vibration and symmetric C−H stretching.[11,23,39] The strong and intense band observed at 1620 cm^{-1} and another band near 1370 cm^{-1} are attributed to the asymmetric and symmetric stretching of the carboxylate groups, respectively,[34,35,38] where weakening of peaks can be observed after the MA-1@CNT was synthesized, and this is attributed to the MA-1's linkage with the carboxylate groups on the surface of the F-CNT. In other bands found at 440 and below 1000 cm^{-1}, respectively, the vibrational modes of metal oxide (O−M−O) and (M−O) are noted, which ensure the coordination of Nd(III) with the oxygen of the CO_2H group on the CNT.[22,40] A group of absorption peaks at 1170 and 1735 cm^{-1} in the FT-IR spectrum of F-CNTs (Figure S1) are designated to the C−O, and C═O stretching vibrations, respectively, and a peak can be seen at 1640 cm^{-1} due to the hydrogen bonding between the OH^- groups. It means that the CNT after acid treatment has been functionalized and some carboxyl groups are bonding with Nd(III) ions to create carboxylates.[23,40,41] Predicated on the FT-IR results, it is possible to deduce that CNTs were effectively adorned with the MA-1 crystal.

3.2.3. SEM and TEM Analysis. The morphology of the MA-1 crystal and MA-1@CNT nanocomposite was characterized using SEM and TEM (Figure 4). As demonstrated in SEM images, Figure 4a reveals that a 3D network of MA-1 has nanorods bounded by six long rectangular faces with precise edges and relatively flat ends. The SEM images have shown that there is a uniform shape for all nanorods within crystals. In the SEM image of MA-1@CNT (Figure 4b), MA-1 nanorods were successfully grown on the F-CNT surface, in which one can see the MA-1 nanorods clearly. The morphology and size of the as-synthesized MA-1 were investigated using TEM (Figure 4c−e); it exhibits a rod-like structure in shape with an average width and length of roughly 20 and 60 nm, respectively.

The TEM image of MA-1@CNT indicates the excellent adhesion between MA-1 nanorods and the F-CNT surface owing to strong electrostatic interactions, which confirms the formation of MA-1@CNT nanohybrids (Figure 4f).

A thorough examination of the distribution of Nd, C, and O on the MA-1@CNT surface can be done using EDS, and the findings are displayed in Figure 5a. The results show that the existence of the elements Nd, C, and O validates the effective synthesis of the hybrid nanocomposite (Figure 5b).

3.3. Description of the Fluorescence Measurements of MA-1@CNT. *3.3.1. Reaction Condition Optimization.* The FL spectra of MA-1@CNT were studied to investigate its potential

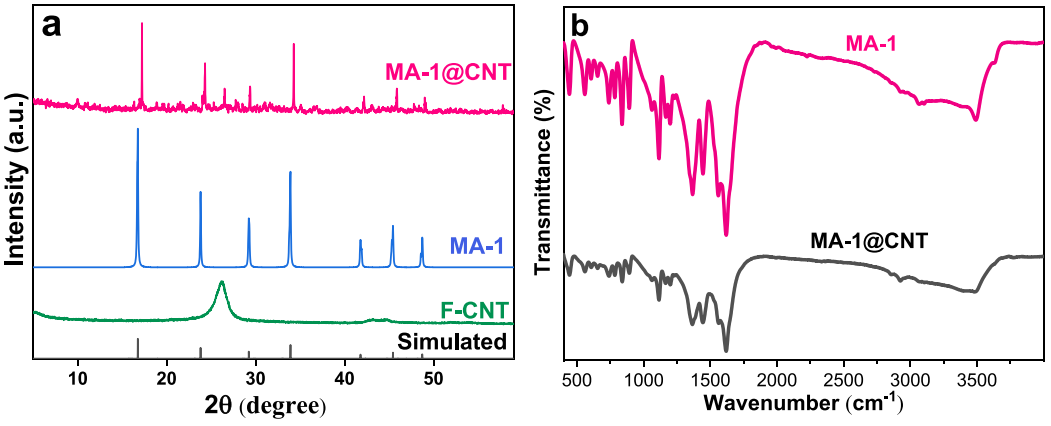

Figure 3. (a) XRD of F-CNT, MA-1, and MA-1@CNT and (b) FT-IR patterns of MA-1 and MA-1@CNT.

https://doi.org/10.1021/acsomega.2c06209
ACS Omega 2023, 8, 1220−1231

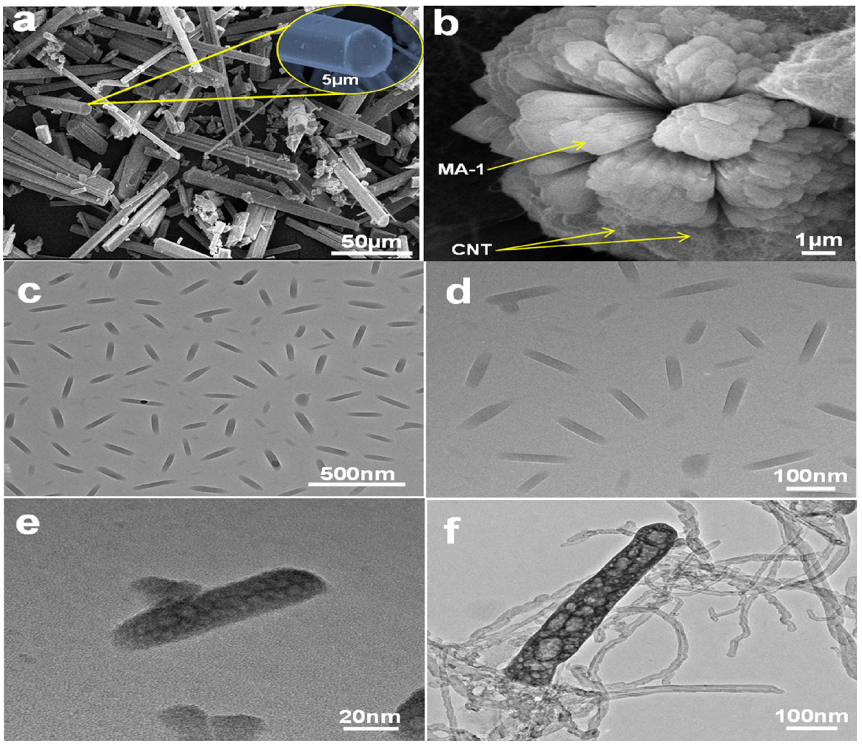

Figure 4. SEM images of (a) MA-1 and (b) MA-1@CNT and TEM images of (c–e) MA-1 and (f) MA-1@CNT.

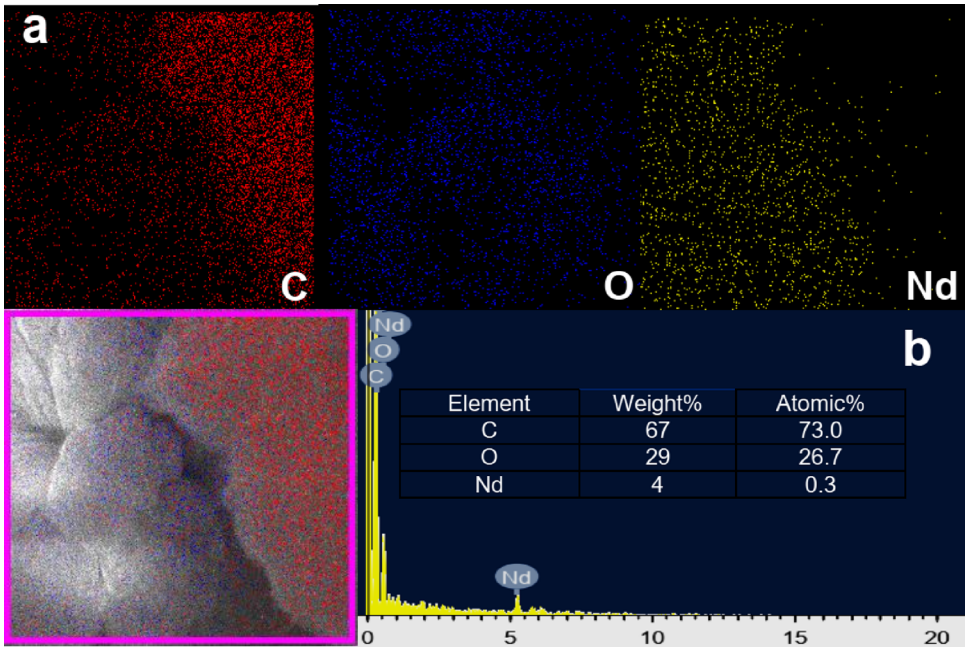

Figure 5. (a) Element mapping of Nd, O, and C of MA-1@CNT nanohybrids. (b) EDAX morphology diagram of MA-1@CNT nanohybrids.

application in detecting Pb(II), As(III), Cr(VI), and NB and to understand the primary mechanism of interaction. The influence of the concentration of MA-1@CNT, various solvents, ionic strength, and pH on the FL spectra was studied. Before the fluorescence study, Pb(II), As(III), Cr(VI), and other NACs, namely, NB, MNB, PNA, and MNA, were prepared in water with different concentrations. MA-1@CNT was ground thoroughly and ultrasonicated after being dissolved in different organic solvents for 15 min and then aged for a day to form a homogeneous suspension. The intensity of the FL increases as the amount of MA-1@CNT increases, and maximum FL intensity was measured at 0.3 mg mL^{-1} concentration of the FL sensor. The emission properties were investigated in numerous solvents. The effect of different solvents like DMF, DMSO, EtOH, MeOH, and H_2O on the FL intensity of MA-1@CNT is shown in Figure 6a. The significant FL intensity of MA-1@CNT showed the highest intensity in the water while affecting other solvents very weakly.

As illustrated in Figure S2, the FL spectra of MA-1@CNT show distinct excitation and emission peaks at 280 and 397 nm,

https://doi.org/10.1021/acsomega.2c06209
ACS Omega 2023, 8, 1220−1231

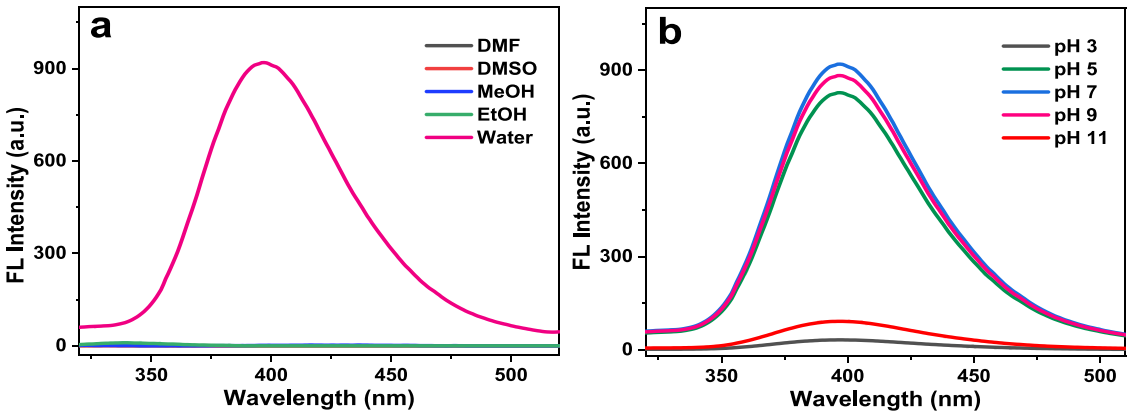

Figure 6. (a) FL spectra of MA-1@CNT in different solvents (0.3 mg/mL). (b) Effect of pH on FL spectra of pure MA-1@CNT (0.3 mg/mL).

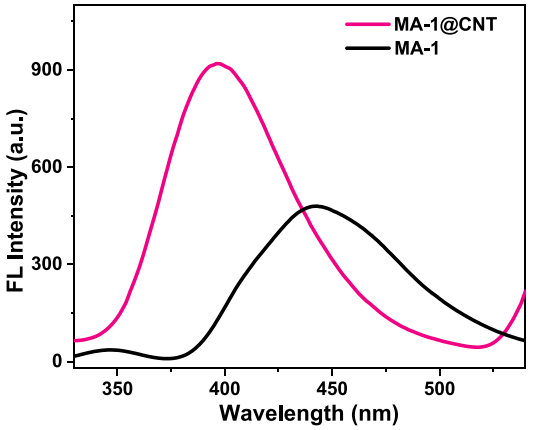

Figure 7. Emission spectra ofMA-1 and MA-1@CNT in DW (pH = 7.0) (0.3 mg/mL), λ_{ex} = 280 nm.

respectively. The effect of ionic strength was analyzed with different concentrations of NaCl, and no such distinguishable effect on FL intensity of PANI@Nd-LDH is observed, as shown in Figure S3a. The FL intensity of pure MA-1@CNT is the maximum at neutral pH (7.0) while decreasing in the base as well as in acidic pH (Figure 6b and Figure S3b). As a result, the sensing tests were conducted under the previously optimized conditions. In many sensing applications, response time plays an important role; therefore, the effect of reaction time between MA-1@CNT and Cr(VI) and NB was also investigated. Figure S4a−d displays the emission band of MA-1@CNT after adding 0.1 ppm Cr(VI), 0.1 ppm As(III), 0.1 ppm Pb(II), and 0.06 ppm NB with varying response times. The intensity decreased with Cr(VI) and NB while increasing in the case of As(III) and Pb(II) with the gradual rise in the incubation time. However, the intensity remained nearly unchanged after 2 min for Cr(VI), 3 min for NB, and 1 min for As(III) and Pb(II).

The fluorescence spectra of pure MA-1 and MA-1@CNT are illustrated in Figure 7. It is noticed that the fluorescence spectrum of MA-1 linked to the CNT is 46 nm blueshifted, and its fluorescence intensity is twice that of MA-1 because the CNTs worked to improve the CP composition and control its properties.[1]

3.3.2. Fluorescence "Turn-Off" Sensing of Cr(VI) and NB. The fluorescent response of MA-1@CNT toward some metal ions (Cr^{3+}, K^{+}, Cu^{2+}, Mg^{2+}, Na^{+}, Co^{2+}, Cd^{2+}, As^{3+}, Pb^{2+}, and Cr^{+6}) and also other NACs (nitrobenzene (NB), *m*-nitrobenzene (MNB), *m*-nitroaniline (MNA), and *p*-nitroaniline (PNA)) was obtained by adding solutions containing various metal ions and other NACs independently to the solution of MA-1@CNT dispersed in deionized water at room temperature. As shown in Figure 8 and Figures S5−S8, adding other metal ions and NACs has a weaker effect on the luminescence than Cr(VI), As(III), Pb(II), and NB. Several paramagnetic metal ions, such as Cu(II), are frequently used as fluorescence quenchers. Ironically, there are a limited number of fluorescent probes available for detecting Cr(VI) in the existence of these paramagnetic metal ions.[40]

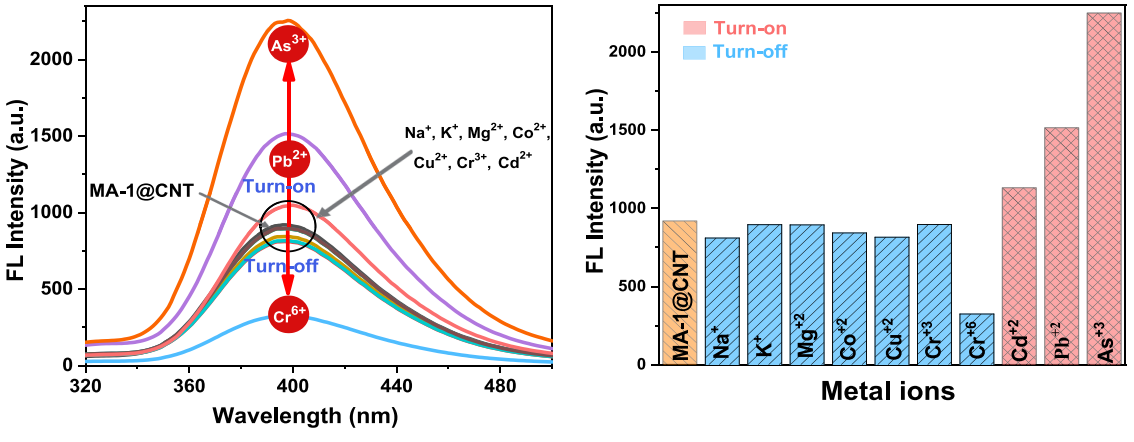

Figure 8. Change in the fluorescence spectrum of MA-1@CNT(0.3 mg/mL) in the presence of different metal ions(0.9 ppm) in DW (pH = 7.0).

https://doi.org/10.1021/acsomega.2c06209
ACS Omega 2023, 8, 1220−1231

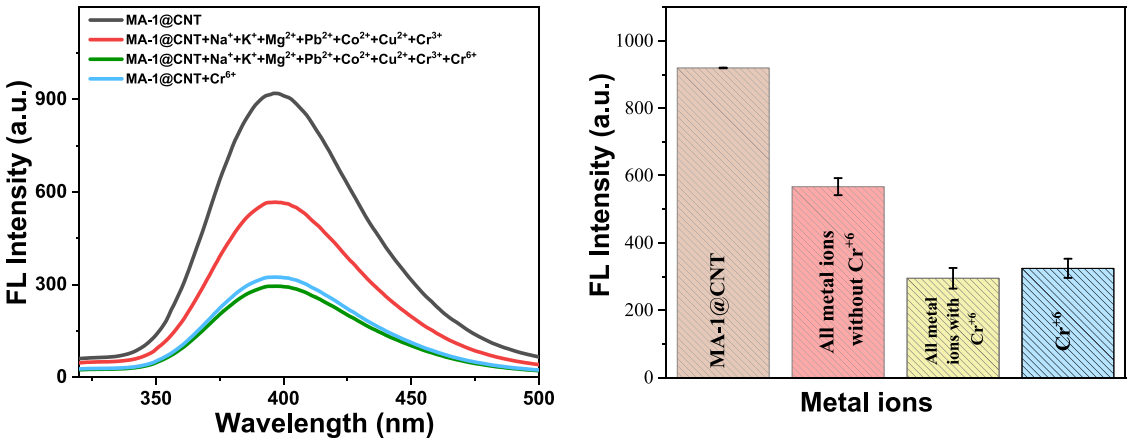

Figure 9. Effect of various metal cations on the selectivity of MA-1@CNT for Cr(VI) detection.

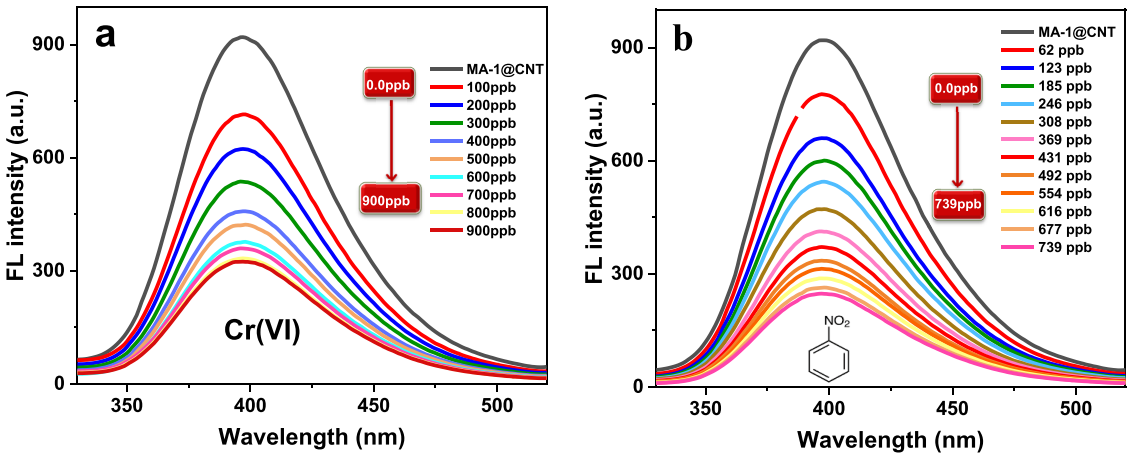

Figure 10. Fluorescence titration spectra of MA-1@CNT (λ_{ex} = 280 nm) in deionized water (0.3 mg/mL) (pH = 7.0) upon gradual addition of (a) Cr(VI) and (b) NB.

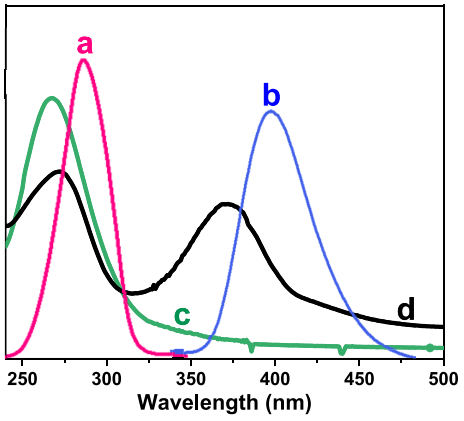

Figure 11. (a) FL excitation, (b) emission spectra of the MA-1@CNTnanocomposite, and UV−vis absorption spectrum of (c) Cr(VI) and (d) NB in water.

Furthermore, the influence of various metal cations was studied [Cr^{3+}, K^+, Cu^{2+}, Mg^{2+}, Na^+, and Co^{2+}] to investigate MA-1@CNT selectivity for Cr(VI) detection. On the other hand, the luminescent intensities of MA-1@CNT suspension were evaluated to study its selectivity in the cation mentioned above in mixtures with/without Cr(VI). As depicted in Figure 9, the intensities were less influenced by other cations but significantly decreased when Cr(VI) was added, which demonstrated that MA-1@CNT has excellent selectivity for Cr(VI) compared to other common cations found in aqueous solutions. In the present work, the MA-1@CNT-based sensor showed no noticeable change in Cr(VI) intensity in the presence of these metal ions.

To further assess the sensitivity of MA-1@CNT toward Cr(VI) ions and NB for sensing, the fluorescence titration tests were carried out with water. Various concentrations of Cr(VI) ranging from 0.1 to 0.9 ppm were tested in this sensitivity study. Figure 10a illustrates that the fluorescence intensity at 397 nm steadily reduced with a rising Cr(VI) concentration. The sensing properties of MA-1@CNT for NB have been studied further through monitoring a series of MA-1@CNT emissions in pH = 7 with a steadily increasing NB concentration. As shown in Figure 10b, the luminescent intensity of the suspended solution of MA-1@CNT gradually decreases with the increasing concentration of NB. The fluorescence intensity may decrease with increased Cr(VI) and NB concentrations because of the inner filter effect (IFE).

In the IFE, the absorption band of the quencher should complementarily overlap with the fluorescent agent's excitation, emission, or both bands,[12,42,43] Cr(VI) displays two notable absorption bands at 270 and 372 nm and a band for NB at 267 nm, as demonstrated in Figure 11.

Meanwhile, the excitation and emission bands of the prepared nanomaterial MA-1@CNT are exhibited at 280 and 397 nm,

https://doi.org/10.1021/acsomega.2c06209
ACS Omega 2023, 8, 1220−1231

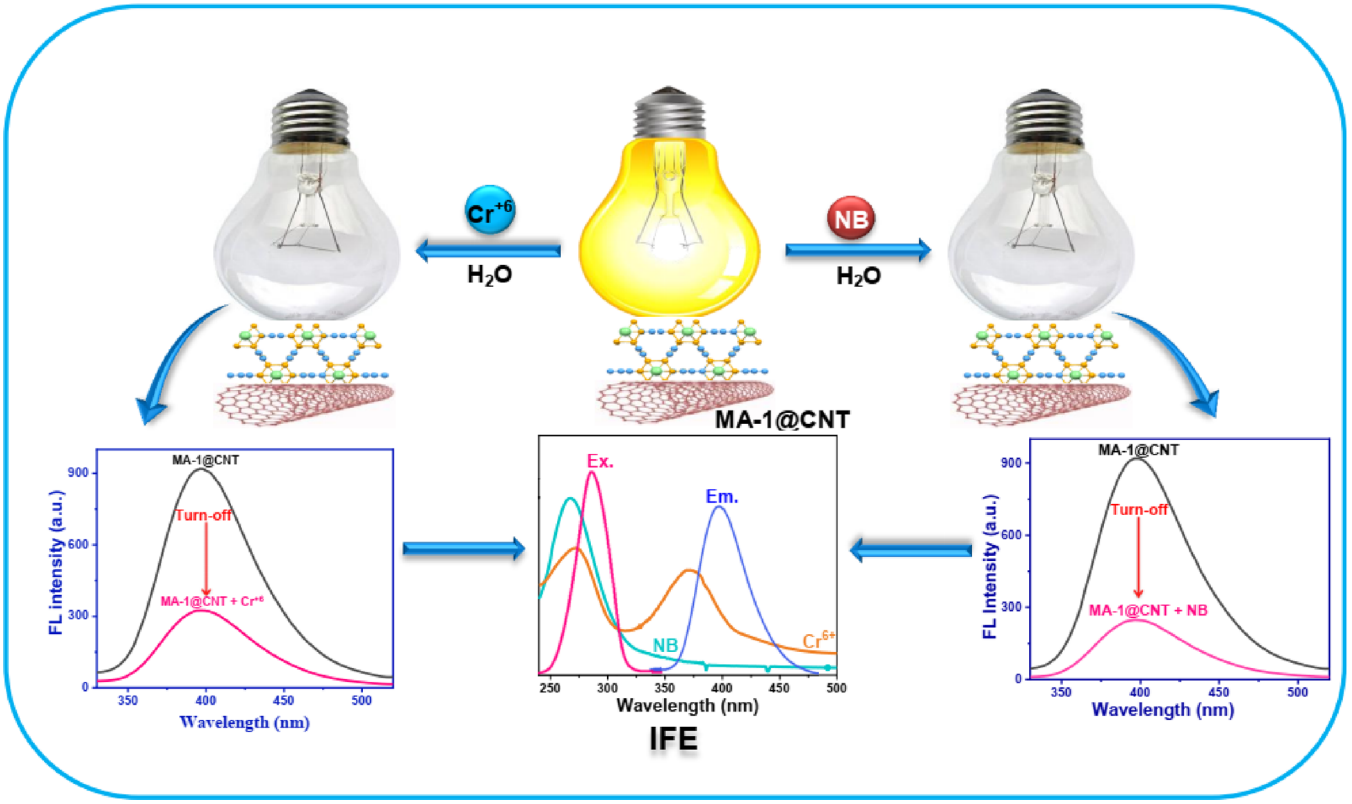

Figure 12. Illustration of MA-1@CNT as a probe for NB and Cr(VI).

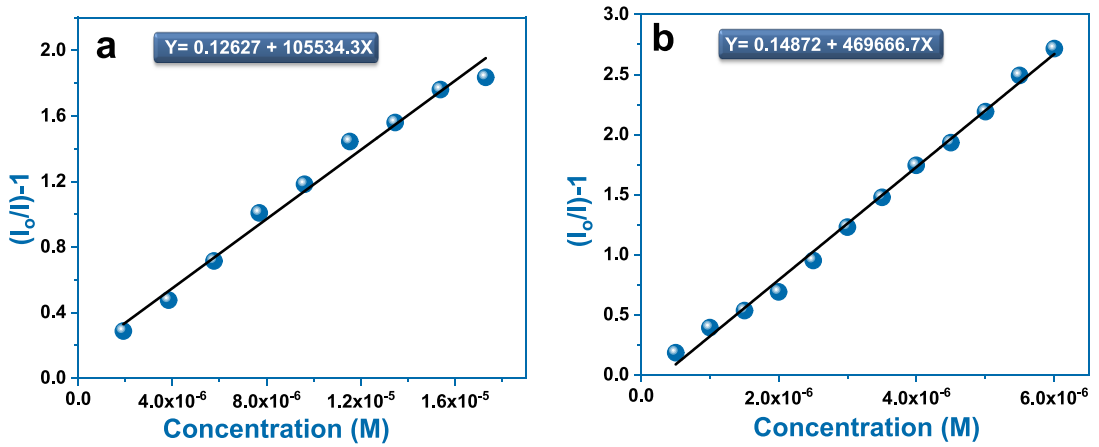

Figure 13. MA-1@CNT SV plots for (a) Cr(VI) and (b) NB.

respectively. This explains the decrease in FL intensity when adding NB and Cr(VI) to the solution of MA-1@CNT (Figure 12).

The Stern–Volmer (SV) equation, $(I_0/I) = K_{SV}[Q] + 1$, was used to investigate the effectiveness of fluorescence quenching, where I_0 and I are the fluorescence intensity before and after the addition of the analyte and [Q] is the analyte's molar concentration. At the same time, K_{SV} is the quenching constant (M^{-1}).[44] The SV plot for Cr(VI), NB, and other NACs were linear with correlation coefficients of 0.986 for Cr(VI), 0.995 for NB, 0.928 for MNB, 0.976 for PNA, and 0.973 and MNA (Figure 13a,b and Figure S9). The quenching constants for Cr(VI), NB, MNB, PNA, and MNA were 1.0×10^5, 4.7×10^5, 1.6×10^5, 1.0×10^5, and 5.8×10^4 M^{-1}, respectively.

The LOD for MA-1@CNT was determined by the equation $3\sigma/m$ (where σ is the standard deviation (SD), while m indicates the slope) (Figure 14a,b, Figure S10, and Tables S3 and S4). The MA-1@CNT exhibited promising LOD values of 7.69×10^{-8} M for Cr(VI), 2.11×10^{-8} M for NB, 2.97×10^{-8}M for MNB, 3.3×10^{-8}M for PNA, and 5.79×10^{-8}M for MNA.

3.3.3. Fluorescence "Turn-On" Sensing of Pb(II) and As(III). The fluorescence titration for the coupling of MA-1@CNT with Pb(II) and As(III) was conducted in a H_2O solution. As depicted in Figure 15a,b, the addition of Pb(II) and As(III) in the solution of MA-1@CNT led to a dramatic enhancement of the emission intensity centered at 397 nm gradually and may be attributed to the chelation enhanced fluorescence (CHEF) effect. The MA-1@CNT-Pb(II) and MA-1@CNT-As(III) complexes of a CHEF effect depend on the photo-induced

https://doi.org/10.1021/acsomega.2c06209
ACS Omega 2023, 8, 1220−1231

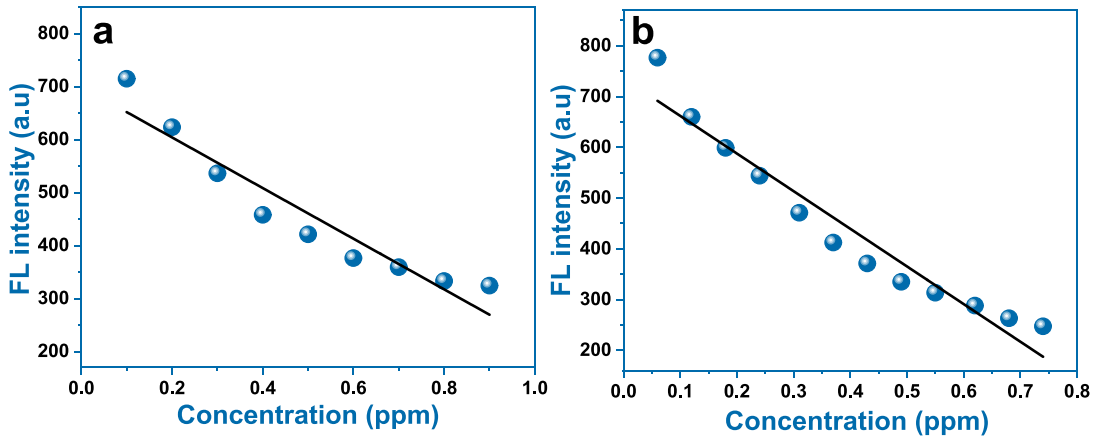

Figure 14. Calculated LOD of MA-1@CNT for (a) Cr(VI) and (b) NB.

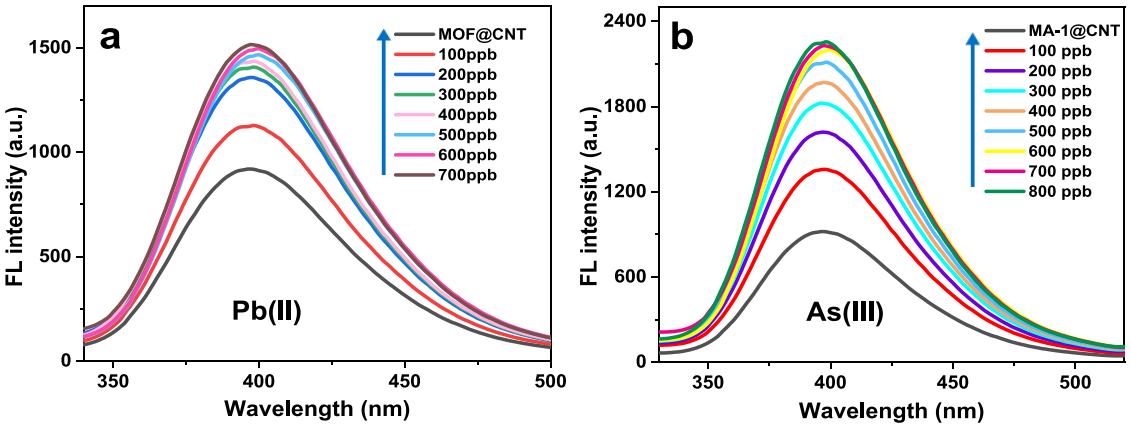

Figure 15. Fluorescence titration spectra of MA-1@CNT (λ_{ex} = 280 nm) in deionized water (0.3 mg/mL) (pH = 7.0) upon addition of gradual (a) Pb(II) and (b) As(III).

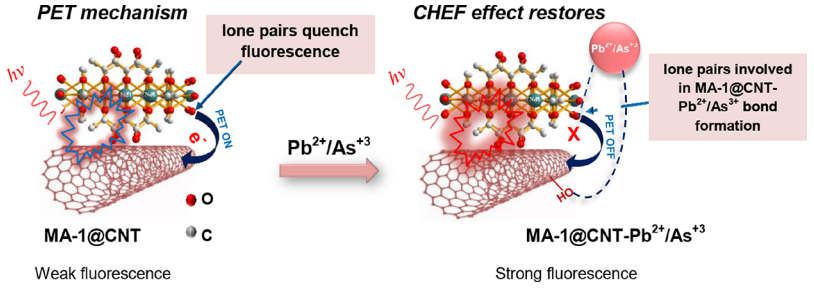

Figure 16. Mechanism of fluorescence enhancement of the complexes MA-1@CNT-Pb(II)/As(III).

electron transfer (PET) mechanism. First, in the PET mechanism, electrons are stimulated in the free MA-1@CNT by the exciting photons to migrate from the lone pairs on donor atoms, such as oxygen atoms of fluorophores, thus resulting in quenching fluorescence. Meanwhile, the existence of the coordinated Pb(II) and As(III) ions in the sensor MA-1@CNT decreases the ion pair's energy, eliminating the PET quenching activity and resulting in the CHEF effect and thus the fluorescence intensity of the MA-1@CNT was sensitive to the concentration change of Pb(II) and As(III), and Figure 16 depicts the suggested binding mechanism.[45,46]

The LOD for MA-1@CNT as a fluorescent chemosensor for analysis of Pb(II) and As(III) was as low as 15.9 and 16.0 nM, respectively (Figures S11a,b and Tables S3 and S4), and this is significantly lower than the USEPA's drinking water standard (Pb(II) = 72 nM and As(III) = 13 M),[47,48] as well as outperforming several prior studies for Pb(II) and As(III) sensing (Table 2), indicating that MA-1@CNT could be used as a fluorescence sensor for Pb(II) and As(III) detection with perfect sensitivity when compared to other related sensors.

3.4. Recycling and Stability. The recyclable performance of MA-1@CNT in Cr(VI) and NB aqueous solutions was also investigated. Fortunately, the MA-1@CNT can be regenerated by centrifuging the suspensions after sensing Cr(VI) ions and NB, thorough washing with water several times, and the quenching efficiencies of three cycles were changed from 65.00 to 60.10% (Cr(VI)) and from 73.30 to 67.90% (NB) as shown in Figure 17a,b, where highly efficient levels were preserved, indicating that MA-1@CNT has high recirculation and stability.

https://doi.org/10.1021/acsomega.2c06209
ACS Omega 2023, 8, 1220−1231

Table 2. Comparisons of Different Fluorometric Sensors for NB, Cr(VI), and As(III)

target	materials	LODs (μM)	linear range (μM)	references
NB	Ni/Al-Fe(CN)$_6$-LDH	0.039	0.067−10	48
	[Zn(HNTB)(phen)]$_n$	753	0−300	49
	UiO-66-NH2	7.30	0−244	50
	Cu(II) MOFs	5.10	13−32	51
	MA-1@CNT	0.021	0.5−6	Current study
Cr(VI)	N, S/C-dots	0.86	1−80	52
	Zn(II) MOFs	6.91	10−10 × 10^3	53
	cobalt(II)-doped CDs	1.170	5−125	54
	Zn^{II}-MOF (TMU-41)	20.0	0−19.2	55
	MA-1@CNT	0.0769	1.9−17.3	Current study
Pb(II)	GQDs-AuNPs	0.0 16	0.5−4	56
	TQ1	0.836	1.6−10	57
	MA-1@CNT	0.0159	0.5−3.4	Current study
As(III)	NH$_2$-MIL-88(Fe)	0.056	0.1−50	58
	Fe$_3$O$_4$-Au core-shell	0.018	0.0−0.27	59
	MA-1@CNT	0.016	1.3−10.6	Current study

4. COMPARATIVE STUDY

A comparative study was made with a previous work. Herein, LODs are lower as compared to the reported earlier NB, Cr(VI), Pb(II), and As(III) sensors as listed in Table 2; hence, we can say that the MA-1@CNT nanocomposite has a good sensing behavior toward NB Cr(VI), Pb(II), and As(III).

5. CONCLUSIONS

In conclusion, this work has presented the effective synthesis of MA-1@CNT hybrid nanocomposites with a unique novel three-dimensional nanoarchitecture [Nd(NO$_3$)$_3$(H$_2$pzdca)]$_n$ via the excellent adhesion of MA-1 particles with F-CNTs under solvothermal conditions by economical and simple methods. Surprisingly, MA-1@CNT works as a tremendous turn-on and turn-off sensor for Pb(II), As(III), Cr(VI), and NB, which have a negative impact on human health. Furthermore, MA-1@CNT hybrid nanocomposites displayed high reusability by washing with water several times. Thus, the present study demonstrates that the MA-1@CNT hybrid nanocomposites might be a promising candidate for the detection of trace Pb(II), As(III), and Cr(VI) ions and NB.

■ ASSOCIATED CONTENT

Supporting Information

The Supporting Information is available free of charge at https://pubs.acs.org/doi/10.1021/acsomega.2c06209.

FT-IR patterns of the F-CNT, excitation and emission spectra of MA-1@CNT CNT; effect of ionic strength on FL intensity of MA-1@CNT and effect of pH on FL intensity of MA-1@CNT; FL spectra of MA-1@CNT aqueous solution after adding 0.1 ppm Cr(VI), 0.06 ppm NB, 0.1 ppm As(III), and 0.1 ppm Pb(II) with different response times; fluorescence titration spectra of MA-1@CNT (λ_{ex} =280 nm) in deionized water upon addition of gradual *m*-nitrobenzene (MNB), *p*-nitroaniline (PNA), and *m*-nitroaniline (MNA); change in the fluorescence spectrum of MA-1@CNT in the presence of NACs deionized water; fluorescence titration spectra of MA-1@CNT (λ_{ex} =280 nm) in deionized water upon addition of gradual Na$^+$, Cu^{2+}, Co^{2+}, K$^+$, Mg^{2+}, and Cr^{3+}; fluorescence titration spectra of MA-1@CNT (λex =280 nm) in deionized upon addition of gradual Cd(II) ion; MA-1@CNT SV plots for *m*-nitrobenzene (MNB), *p*-nitroaniline (PNA), and *m*-nitroaniline (MNA); calculated LOD of MA-1@CNT for *m*-nitrobenzene (MNB), *p*-nitroaniline (PNA), and *m*-nitroaniline (MNA); calculate LOD of MA-1@CNT for Pb(II) and As(III); selected bond lengths and angles for MA-1; calculation of standard deviation (σ) for MA-1@CNT; and calculation of limit of detection (LOD) for MA-1@CNT (PDF)

■ AUTHOR INFORMATION

Corresponding Author

Amjad Mumtaz Khan − *Department of Chemistry, Aligarh Muslim University, Aligarh 202002, India;* orcid.org/0000-0002-3037-2257; Email: amjadmtkhan96@gmail.com

Authors

Mansour A.S. Salem − *Department of Chemistry, Aligarh Muslim University, Aligarh 202002, India; Department of Chemistry, University of Aden, Aden 6312, Yemen*

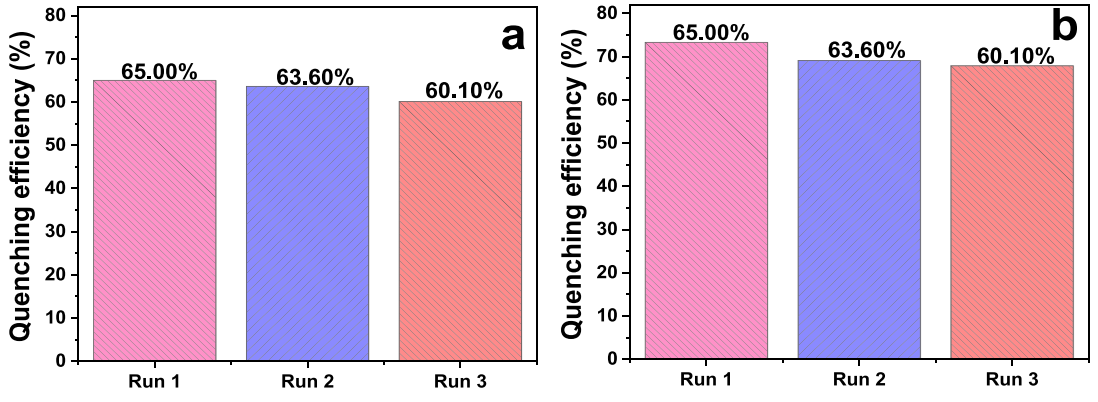

Figure 17. Fluorescence quenching efficiency of three recyclable experiments for (a) Cr(VI) and (b)NB.

https://doi.org/10.1021/acsomega.2c06209
ACS Omega 2023, 8, 1220−1231

Yahiya Kadaf Manea − *Department of Chemistry, University of Aden, Aden 6312, Yemen;* orcid.org/0000-0002-0029-3646
Hatem A.M. Saleh − *Department of Chemistry, Aligarh Muslim University, Aligarh 202002, India*
Musheer Ahmad − *Department of Applied Chemistry (ZHCET), Aligarh Muslim University, Aligarh 202002, India;* orcid.org/0000-0002-7446-0232

Complete contact information is available at: https://pubs.acs.org/10.1021/acsomega.2c06209

Notes

The authors declare no competing financial interest.

■ ACKNOWLEDGMENTS

The authors would like to gratefully acknowledge the Department of Chemistry, University Sophisticated Instrument Facility (USIF), AMU, Aligarh for providing an instrumental facility.

■ REFERENCES

(1) Jabbari, V.; Veleta, J. M.; Zarei-Chaleshtori, M.; Gardea-Torresdey, J.; Villagrán, D. Green Synthesis of Magnetic MOF@GO and MOF@CNT Hybrid Nanocomposites with High Adsorption Capacity towards Organic Pollutants. *Chem. Eng. J.* **2016**, *304*, 774−783.
(2) Manea, Y. K.; Khan, A. M.; Wani, A. A.; Qashqoosh, M. T. A.; Shahadat, M.; Salem, M. A. S. Hydrothermally Synthesized Mesoporous CS-g-PA@TSM Functional Nanocomposite for Efficient Photocatalytic Degradation of Ciprofloxacin and Treatment of Metal Ions. *J. Mol. Liq.* **2021**, *335*, No. 116144.
(3) Rong, M.; Lin, L.; Song, X.; Wang, Y.; Zhong, Y.; Yan, J.; Feng, Y.; Zeng, X.; Chen, X. Fluorescence Sensing of Chromium (VI) and Ascorbic Acid Using Graphitic Carbon Nitride Nanosheets as a Fluorescent "Switch". *Biosens. Bioelectron.* **2015**, *68*, 210−217.
(4) Alahdal, F. A. M.; Qashqoosh, M. T. A.; Kadaf Manea, Y.; Salem, M. A. S.; Hasan Khan, R.; Naqvi, S. Ultrafast Fluorescent Detection of Hexavalent Chromium Ions, Catalytic Efficacy and Antioxidant Activity of Green Synthesized Silver Nanoparticles Using Leaf Extract of P. Austroarabica. *Environ. Nanotechnol., Monit. Manage.* **2022**, *17*, No. 100665.
(5) Ou, B.; Wang, J.; Wu, Y.; Zhao, S.; Wang, Z. Efficient removal of Cr (VI) by magnetic and recyclable calcined CoFe-LDH/g-C_3N_4 via the synergy of adsorption and photocatalysis under visible light. *Chem. Eng. J.* **2020**, *380*, No. 122600.
(6) Manea, Y. K.; Khan, A. M.; Wani, A. A.; Saleh, M. A. S.; Qashqoosh, M. T. A.; Shahadat, M.; Rezakazemi, M. In-Grown Flower like Al-Li/Th-LDH@CNT Nanocomposite for Enhanced Photocatalytic Degradation of MG Dye and Selective Adsorption of Cr (VI). *J. Environ. Chem. Eng.* **2022**, *10*, No. 106848.
(7) Reddy, K. J.; McDonald, K. J.; King, H. A Novel Arsenic Removal Process for Water Using Cupric Oxide Nanoparticles. *J. Colloid Interface Sci.* **2013**, *397*, 96−102.
(8) Priyadarshni, N.; Nath, P.; Nagahanumaiah; Chanda, N. DMSA-Functionalized Gold Nanorod on Paper for Colorimetric Detection and Estimation of Arsenic (III and V) Contamination in Groundwater. *ACS Sustainable Chem. Eng.* **2018**, *6*, 6264−6272.
(9) Alghamdi, A. A.; Al-Odayni, A. B.; Saeed, W. S.; Al-Kahtani, A.; Alharthi, F. A.; Aouak, T. Efficient Adsorption of Lead (II) from Aqueous Phase Solutions Using Polypyrrole-Based Activated Carbon. *Materials* **2019**, *12*, 2020.
(10) Velmurugan, M.; Karikalan, N.; Chen, S.-M.; Dai, Z.-C. Studies on the influence of β-cyclodextrin on graphene oxide and its synergistic activity to the electrochemical detection of nitrobenzene. *J. Colloid Interface Sci.* **2017**, *490*, 365−371.
(11) Salem, M. A. S.; Khan, A. M.; Manea, Y. K. A Novel Nano-Hybrid Carbon Architecture as Chemo Sensor for Natural Hazards: Active Adsorption of Rose Bengal Dye and Detection of Hazard Pollutants at Ppb Level. *J. Environ. Chem. Eng.* **2022**, *10*, No. 107032.
(12) Park, M. K.; Lim, K. S.; Park, J. H.; Song, J. H.; Kang, D. W.; Lee, W. R.; Hong, C. S. Two- and Three-Dimensional Zn(II) Coordination Polymers Constructed from Mixed Ligand Systems: Interpenetration, Structural Transformation and Sensing Behavior. *CrystEngComm* **2016**, *18*, 4349−4358.
(13) He, H.; Song, Y.; Sun, F.; Zhao, N.; Zhu, G. Sorption Properties and Nitroaromatic Explosives Sensing Based on Two Isostructural Metal - Organic Frameworks. *Cryst. Growth Des.* **2015**, *15*, 2033−2038.
(14) Kadaf Manea, Y.; Banu, A.; Qashqoosh, M. T. A.; Mumtaz Khan, A.; Alahdal, F. M. A.; Ahmad Wani, A.; Salem, M. A. S.; Naqvi, S. Interaction of AMOT@CS NPs and AMOT Drug with Bovine Serum Albumin: Insights from Spectroscopic and Molecular Docking Techniques. *Chem. Phys.* **2021**, *546*, No. 111139.
(15) Alahdal, F. A. M.; Qashqoosh, M. T. A.; Manea, Y. K.; Salem, M. A. S.; Khan, A. M. T.; Naqvi, S. Eco-Friendly Synthesis of Zinc Oxide Nanoparticles as Nanosensor, Nanocatalyst and Antioxidant Agent Using Leaf Extract of P. Austroarabica. *OpenNano* **2022**, *8*, No. 100067.
(16) Singh, M.; Kumar, G.; Neogi, S. Devising Mixed-Ligand Based Robust Cd(II)-Framework From Bi-Functional Ligand for Fast Responsive Luminescent Detection of Fe3+ and Cr(VI) Oxo-Anions in Water With High Selectivity and Recyclability. *Front. Chem.* **2021**, *9*, 1−12.
(17) Das, P.; Mandal, S. K. Strategic Design and Functionalization of an Amine-Decorated Luminescent Metal Organic Framework for Selective Gas/Vapor Sorption and Nanomolar Sensing of 2,4,6-Trinitrophenol in Water. *ACS Appl. Mater. Interfaces* **2018**, *10*, 25360−25371.
(18) Pal, A.; Chand, S.; Senthilkumar, S.; Neogi, S.; Das, M. C. Structural Variation of Transition Metal Coordination Polymers Based on Bent Carboxylate and Flexible Spacer Ligand: Polymorphism, Gas Adsorption and SC-SC Transmetallation. *CrystEngComm* **2016**, *18*, 4323−4335.
(19) Bowers, G. M.; Bowers, R. A. Dual-Functionalization Actuated Trimodal Attribute in Ultra-Robust MOF: Exceptionally Selective Capture and Effectual Fixation of CO2 with Fast- View Article Online DOI: 10.1039/D0QM00721H Responsive, Nanomolar Detection of Assorted Organo-Contaminants In. *Underst. Chem. through Cars*; Taylor & Francis 2020, 144−163. DOI: 10.1039/D0QM00721H.Volume.
(20) Iman, K.; Shahid, M.; Khan, M. S.; Ahmad, M.; Sama, F. Topology, Magnetism and Dye Adsorption Properties of Metal Organic Frameworks (MOFs) Synthesized from Bench Chemicals. *CrystEngComm* **2019**, *21*, 5299−5309.
(21) Salama, R. S.; Samra, S. E.; Ahmed, A. I.; El-Hakam, S. A.; Samra, S. E.; El-Dafrawy, S. M. Adsorption, Equilibrium and Kinetic Studies on the Removal of Methyl Orange Dye from Aqueous Solution by the Use of Copper Metal Organic Framework (Cu-BDC) 4 PUBLICATIONS 4 CITATIONS SEE PROFILE Adsorption, Equilibrium and Kinetic Studies on the Removal O. *Int. J. Mod. Chem.* **2018**, *10*, 195−207.
(22) Salem, M. A. S.; Khan, A. M.; Manea, Y. K.; Wani, A. A. Nano Chromium Embedded in F-CNT Supported CoBi-LDH Nanocomposites for Selective Adsorption of Pb2+and Hazardous Organic Dyes. *Chemosphere* **2022**, *289*, No. 133073.
(23) Wang, X.; Yang, N.; Li, Q.; He, F.; Yang, Y.; Wu, B.; Chu, J.; Zhou, A.; Xiong, S. Solvothermal Synthesis of Flower-String-like NiCo-MOF/MWCNT Composites as a High-Performance Supercapacitor Electrode Material. *J. Solid State Chem.* **2019**, *277*, 575−586.
(24) Lin, R.; Ge, L.; Liu, S.; Rudolph, V.; Zhu, Z. Mixed-Matrix Membranes with Metal-Organic Framework-Decorated CNT Fillers for Efficient CO2 Separation. *ACS Appl. Mater. Interfaces* **2015**, *7*, 14750−14757.
(25) Shen, C.-H.; Chuang, C.-H.; Gu, Y.-J.; Ho, W.-H.; Song, Y.-D.; Chen, Y.-C.; Wang, Y.-C.; Kung, C.-W. Cerium-Based Metal-Organic Framework Nanocrystals Interconnected by Carbon Nanotubes for Boosting Electrochemical Capacitor Performance. *ACS Appl. Mater. Interfaces* **2021**, *13*, 16418−16426.

(26) Hwang, Y. K.; Hong, D.-Y.; Chang, J.-S.; Jhung, S. H.; Seo, Y.-K.; Kim, J.; Vimont, A.; Daturi, M.; Serre, C.; Férey, G. Amine Grafting on Coordinatively Unsaturated Metal Centers of MOFs: Consequences for Catalysis and Metal Encapsulation. *Angew. Chem., Int. Ed.* **2008**, *120*, 4212−4216.
(27) Eddaoudi, M.; Kim, J.; Rosi, N.; Vodak, D.; Wachter, J.; O'Keeffe, M.; Yaghi, O. M. Systematic Design of Pore Size and Functionality in Isoreticular MOFs and Their Application in Methane Storage. *Science* **2002**, *295*, 469−472.
(28) Petit, C.; Bandosz, T. J. MOF-Graphite Oxide Composites: Combining the Uniqueness of Graphene Layers and Metal-Organic Frameworks. *Adv. Mater.* **2009**, *21*, 4753−4757.
(29) Kim, M.; Cahill, J. F.; Fei, H.; Prather, K. A.; Cohen, S. M. Postsynthetic Ligand and Cation Exchange in Robust Metal-Organic Frameworks. *J. Am. Chem. Soc.* **2012**, *134*, 18082−18088.
(30) Thornley, P. A. The Synthesis and Characterisation of a Novel Polyamine-Terpyridine Ligand and Related Complexes By. *J. Am. Chem. Soc.* **2009**, *102*, 10662−10669.
(31) Work, W. J.; Horie, K.; Hess, M.; Stepto, R. F. T. Definition of Terms Related to Polymer Blends, Composites, and Multiphase Polymeric Materials (IUPAC Recommendations 2004). In *Pure and Applied Chemistry*; De Gruyter 2004; Vol. *76*, pp. 1985−2007. DOI: 10.1351/pac200476111985.
(32) Ostermann, R.; Cravillon, J.; Weidmann, C.; Wiebcke, M.; Smarsly, B. M. Metal-Organic Framework Nanofibers via Electrospinning. *Chem. Commun.* **2011**, *47*, 442−444.
(33) Abdi, J.; Vossoughi, M.; Mahmoodi, N. M.; Alemzadeh, I. Synthesis of Metal-Organic Framework Hybrid Nanocomposites Based on GO and CNT with High Adsorption Capacity for Dye Removal. *Chem. Eng. J.* **2017**, *326*, 1145−1158.
(34) Wang, F.; Chen, X.; Chen, L.; Yang, J.; Wang, Q. High-performance non-enzymatic glucose sensor by hierarchical flower-like nickel(II)-based MOF/carbon nanotubes composite. *Mater. Sci. Eng., C* **2019**, *96*, 41−50.
(35) Ahsan, M. A.; Jabbari, V.; Islam, M. T.; Turley, R. S.; Dominguez, N.; Kim, H.; Castro, E.; Hernandez-viezcas, J. A.; Curry, M. L.; Lopez, J.; Gardea-torresdey, J. L.; Noveron, J. C. Science of the Total Environment Sustainable Synthesis and Remarkable Adsorption Capacity of MOF / Graphene Oxide and MOF/CNT Based Hybrid Nanocomposites for the Removal of Bisphenol A from Water. *Sci. Total Environ.* **2019**, *673*, 306−317.
(36) Dolomanov, O. V.; Bourhis, L. J.; Gildea, R. J.; Howard, J. A. K.; Puschmann, H. *OLEX2*: A Complete Structure Solution, Refinement and Analysis Program. *J. Appl. Crystallogr.* **2009**, *42*, 339−341.
(37) Bourhis, L. J.; Dolomanov, O. V.; Gildea, R. J.; Howard, J. A.; Puschmann, H. The Anatomy of a Comprehensive Constrained, Restrained Refinement Program for the Modern Computing Environment − *Olex2* Dissected. *Acta Cryst.* **2015**, *71*, 59−75.
(38) Yaqoob, L.; Noor, T.; Iqbal, N.; Nasir, H.; Zaman, N.; Talha, K. Electrochemical synergies of Fe−Ni bimetallic MOF CNTs catalyst for OER in water splitting. *J. Alloys Compd.* **2021**, *850*, No. 156583.
(39) Ran, F.; Yang, X.; Xu, X.; Bai, Y.; Shao, L. Boosting the Charge Storage of Layered Double Hydroxides Derived from Carbon Nanotube-Tailored Metal Organic Frameworks. *Electrochim. Acta* **2019**, *301*, 117−125.
(40) Wani, A. A.; Khan, A. M.; Manea, Y. K.; Salem, M. A. S.; Shahadat, M. Selective Adsorption and Ultrafast Fluorescent Detection of Cr(VI) in Wastewater Using Neodymium Doped Polyaniline Supported Layered Double Hydroxide Nanocomposite. *J. Hazard. Mater.* **2021**, *416*, No. 125754.
(41) Yang, J.; Yu, C.; Fan, X.; Ling, Z.; Qiu, J.; Gogotsi, Y. Facile Fabrication of MWCNT-Doped NiCoAl-Layered Double Hydroxide Nanosheets with Enhanced Electrochemical Performances. *J. Mater. Chem. A* **2013**, *1*, 1963−1968.
(42) Sun, X. Y.; Yuan, M. J.; Liu, B.; Shen, J. S. Carbon Dots as Fluorescent Probes for Detection of VB_{12} Based on the Inner Filter Effect. *RSC Adv.* **2018**, *8*, 19786−19790.
(43) Chen, S.; Yu, Y. L.; Wang, J. H. Inner Filter Effect-Based Fluorescent Sensing Systems: A Review. *Analytica Chimica Acta.*; Elsevier B.V. 2018, pp. 13−26. DOI: 10.1016/j.aca.2017.10.026.
(44) Instrumentation for Fluorescence Spectroscopy. In *Principles of Fluorescence Spectroscopy*; Springer: Boston, MA, 2006; pp. 27−61. DOI: 10.1007/978-0-387-46312-4_2.
(45) Lan, L.; Niu, Q.; Guo, Z.; Liu, H.; Li, T. *Highly Sensitive and Fast Responsive "Turn-on" Fluorescent Sensor for Selectively Sensing Fe3+ and Hg2+ in Aqueous Media Based on an Oligothiophene Derivative and Its Application in Real Water Samples*; Elsevier B.V., 2017. DOI: 10.1016/j.snb.2017.01.042.
(46) Zhu, W.; Yang, L.; Fang, M.; Wu, Z.; Zhang, Q.; Yin, F. New Carbazole-Based Schiff Base : Colorimetric Chemosensor for Fe^{3+} and fluorescent Turn-on Chemosensor for Fe^{3+} and Cr^{3+}. *J. Lumin.* **2015**, *158*, 38−43.
(47) WQA. *WQA Technical Fact Sheet: Arsenic.*; Water Qual. Association 2013.
(48) Amini, R.; Rahimpour, E.; Jouyban, A. An Optical Sensing Platform Based on Hexacyanoferrate Intercalated Layered Double Hydroxide Nanozyme for Determination of Chromium in Water. *Anal. Chim. Acta* **2020**, *1117*, 9−17.
(49) Yang, H.; Qi, D.; Chen, Z.; Cao, M.; Deng, Y.; Liu, Z.; Shao, C.; Yang, L. A Zn-based metal−organic framework as bifunctional chemosensor for the detection of nitrobenzene and Fe^{3+}. *J. Solid State Chem.* **2021**, *296*, No. 121970.
(50) Vellingiri, K.; Boukhvalov, D. W.; Kumar, S.; Deep, A.; Kim, K. Luminescent Metal-Organic Frameworks for the Detection of Nitrobenzene in Aqueous Media. *Sens. Actuators, B* **2017**, *245*, 305−313.
(51) Ahamad, M. N.; Shahid, M.; Ahmad, M.; Sama, F. Cu(II) MOFs Based on Bipyridyls: Topology, Magnetism, and Exploring Sensing Ability toward Multiple Nitroaromatic Explosives. *ACS Omega* **2019**, *4*, 7738−7749.
(52) Chen, J.; Liu, J.; Li, J.; Xu, L.; Qiao, Y. One-Pot Synthesis of Nitrogen and Sulfur Co-Doped Carbon Dots and Its Application for Sensor and Multicolor Cellular Imaging. *J. Colloid Interface Sci.* **2017**, *485*, 167−174.
(53) Jin, H.; Xu, J.; Zhang, L.; Ma, B.; Shi, X.; Fan, Y.; Wang, L. Multi-Responsive Luminescent Sensor Based on Zn (II) Metal-Organic Framework for Selective Sensing of Cr(III), Cr(VI) Ions and p-Nitrotolune. *J. Solid State Chem.* **2018**, *268*, 168−174.
(54) Zhang, H.-Y.; Wang, Y.; Xiao, S.; Wang, H.; Wang, J.-H.; Feng, L. Rapid detection of Cr(VI) ions based on cobalt(II)-doped carbon dots. *Biosens. Bioelectron.* **2017**, *87*, 46−52.
(55) Abdollahi, N.; Morsali, A. Highly sensitive fluorescent metal-organic framework as a selective sensor of Mn^{VII} and Cr^{VI} anions (MnO_4^-/$Cr_2O_7^{2-}$/CrO_4^{2-}) in aqueous solutions. *Anal. Chim. Acta* **2019**, *1064*, 119−125.
(56) Niu, X.; Zhong, Y.; Chen, R.; Wang, F.; Liu, Y.; Luo, D. A "Turn-on" Fluorescence Sensor for Pb^{2+} Detection Based on Graphene Quantum Dots and Gold Nanoparticles. *Sens. Actuators, B* **2018**, *255*, 1577−1581.
(57) Liu, T.; Wan, X.; Yao, Y. Dual Sensitive and Selective Sensor for Pb^{2+} and Al^{3+} with Distinctive Fluorescence Response. *Sens. Actuators, B* **2018**, *254*, 1094−1100.
(58) Xie, D.; Ma, Y.; Gu, Y.; Zhou, H.; Zhang, H.; Wang, G.; Zhang, Y.; Zhao, H. Bifunctional NH2-MIL-88(Fe) Metal-Organic Framework Nanooctahedra for Highly Sensitive Detection and Efficient Removal of Arsenate in Aqueous Media. *J. Mater. Chem. A* **2017**, *5*, 23794−23804.
(59) Banerjee, S.; Kumar, N. P.; Srinivas, A.; Roy, S. Core-Shell Fe_3O_4@Au Nanocomposite as Dual-Functional Optical Probe and Potential Removal System for Arsenic (III)from Water. *J. Hazard. Mater.* **2019**, *375*, 216−223.

https://doi.org/10.1021/acsomega.2c06209
ACS Omega 2023, 8, 1220−1231